Positioning, 2026, 17(3), 21-38
https://www.scirp.org/journal/pos
ISSN Online: 2150-8526
ISSN Print: 2150-850X

Enhanced Measurements of GPS Transmissivity through a Light Rain Event

Mark D. Jacobson[1], Ayjeren Kossekova[2]

[1]Department of Mathematics, Montana State University Billings, Billings, MT, USA
[2]Independent Researcher, New York City, NY, USA
Email: mjacobson@msubillings.edu

How to cite this paper: Jacobson, M.D. and Kossekova, A. (2026) Enhanced Measurements of GPS Transmissivity through a Light Rain Event. *Positioning*, **17**, 21-38.
https://doi.org/10.4236/pos.2026.173003

Received: July 8, 2026
Accepted: August 8, 2026
Published: August 11, 2026

Abstract

Received Global Positioning System (GPS) signals through a light rain event are measured for 8 GPS satellites. The incident GPS signals are at 1.57542 GHz with right-hand circular polarization (RHCP). The power transmission of GPS signals to the receiver is referred to as GPS Transmissivity (GPS-T). Using 8 GPS orbital tracks improves the spatial and temporal resolution of the GPS-T measurements through the light rain event compared to using only 1 GPS orbital track. In this analysis, the normalized antenna elevation gain pattern is included. However, the normalized antenna azimuth gain pattern is not included because it is assumed to be approximately constant. The relative received powers through the light rain are measured with an antenna that is covered by a fiberglass hemispherical radome. The water-layer's power transmission loss on the radome (0.05 dB) is neglected because it is much less than the minimum measured power transmission losses during the light rain (~0.5 dB). Furthermore, the radome's power transmission loss is eliminated by subtracting the received power during the light rain from the received power when the radome surface is dry during the mostly clear skies overhead. The measured power transmission losses and transmissivities (power transmissions) through the light rain for 8 GPS satellites are shown in 16 plots. In addition, the temporal and spatial variability of these measurements are shown in 2 animations. The impact of these results on GPS operational applications during rain and on potentially detecting ice crystals is discussed.

Keywords

Global Positioning System, Power Transmission, Transmissivity, Power Transmission Loss, Right-Hand Circular Polarization, Light Rain, Radome

1. Introduction

The power transmission of Global Positioning System (GPS) signals to the receiver is referred to as GPS Transmissivity (GPS-T) [1]. This includes conditions when GPS signals propagate through rain. The power transmission of GPS signals through rain is degraded by both attenuation and depolarization. Rain attenuation is usually neglected at the Global Navigation Satellite Systems (GNSS) frequencies for rain rates up to 30 mm·h^{-1} [2]. Furthermore, for L-band, the rain attenuation is less than 0.1 dB·km^{-1} for a rain rate of 150 mm·h^{-1} [3], [4]. In contrast, for frequencies of 4 GHz and below, circularly polarized signals through rain are degraded significantly more by depolarization than by attenuation [5]-[7].

In the previous GPS-T paper by Jacobson [1], received GPS azimuth angles (AZ) were restricted to 180˚ ≤ AZ ≤ 360˚ for minimizing blockage at the site, where AZ = 360˚ = 0˚ is True North. Furthermore, received GPS elevation angles (EL) were restricted to 65˚ ≤ EL ≤ 90˚ for providing constant antenna gain, where EL = 90˚ is Zenith. GPS satellite SV (PRN) 29 was chosen among the available GPS satellites of the constellation for these measurements because it had the only orbital track that met the azimuth and elevation angle criteria. These criteria were critical to minimize the degradation of the received GPS signals by blockage and antenna gain.

In this paper, the normalized antenna elevation gain pattern is included for 8 received GPS signals. In contrast, the normalized antenna azimuth gain pattern is not included because it is assumed to be approximately constant. The GPS-T measurements presented here include both rain depolarization and rain attenuation for light rain (rain rate < 2.5 mm·h^{-1} [8]) for 8 GPS satellites. Using 8 GPS orbital tracks improves the spatial and temporal resolution of the GPS-T measurements through the light rain event compared to using only 1 GPS orbital track in [1]. The goal of the GPS-T measurements is to better understand and to quantify how light rain affects GPS signals over land.

2. Receiving Antenna Characteristics

Recently, a Trimble (Sunnyvale, CA, USA) Lassen LP GPS L1 (1.57542 GHz right-hand circularly polarized (RHCP) antenna) receiver was used to measure GPS signal strengths through a light rain event [1]. The active Trimble antenna consists of a microstrip patch antenna (20 mm × 20 mm × 1.6 mm), a preamplifier, a radome, and a ground plane. See **Table 1** for the GPS antenna specifications [9]. The preamplifier circuit amplifies the noise-like GPS spread spectrum signal. The receiver is a standard closed loop type. Power levels were directly recorded in dB from the GPS receiver every 1 s to a laptop computer.

In this analysis, the absolute value of the normalized antenna elevation gain (relative received power) pattern is added to the received GPS signals, see (1) and **Figure 1** below. In contrast, the normalized antenna azimuth gain pattern is not added to the received GPS signals because it is assumed to be approximately constant. This is a reasonable assumption since the normalized elevation gain patterns for azimuth angles of 0˚ and 90˚ from 3 different Trimble Lassen LP GPS L1 antennas (given by Trimble's data sheets) are within 1 dB. The normalized elevation gain pattern is obtained by averaging the antenna elevation patterns from 3 different Trimble Lassen LP GPS L1 antennas. The averaging of these elevation gain patterns is accomplished by the following method:

Table 1. Specifications for the GPS receiving antenna [9].

Specification	Value
Frequency range	1575.42 ± 1.023 MHz
Gain	+3.0 dBi, minimum at 90˚ −4.0 dBi, minimum at 20˚
Polarization	RHCP
Axial ratio	+4.0 dB, maximum at 90˚ +6.0 dB, maximum at 10˚
Half-power beamwidth	140˚
Front-to-back ratio	+15 dB

- for an azimuth of 0˚, the normalized elevation gain pattern for one antenna is discretized every 10˚ for $-90^{\circ} \leq \text{off axis} \leq +90^{\circ}$.
- the normalized gains for each pair of ± elevation angles (approximately symmetrical) are averaged to a single normalized gain for the + elevation angle.
- the above process is repeated for an azimuth of 90˚.
- the above process is repeated for the other two antennas.
- the three normalized gains for each + elevation angle are averaged to a single normalized gain.
- an exponential regression is performed with the elevation gain pattern from 0˚ - 90˚.

The regression equation is

$$\text{RRP}(\text{OA}) = -9.009 \cdot e^{-0.033 \cdot |\text{OA}|} + 0.614 \quad (1)$$

where

RRP = Relative Received Power, the normalized antenna elevation gain (dB)

OA = Off Axis angle (degrees).

Figure 1 shows the average relative received elevation power pattern for the GPS antenna in rectangular form, where the relative power pattern is symmetrical about 0˚.

3. Measurements during Light Rain

3.1. Location and Setup for Measurements

On June 2, 2025, from 6:21 p.m. - 6:48 p.m. Greenwich Mean Time (GMT), also known as Universal Time (UT), the GPS receiver from Section 2 was used to measure the GPS signals through the light rain [1]. A 61-cm-diameter, 3-mm-thick fiberglass hemispherical radome was leveled and centered over the horizontally mounted GPS antenna to keep it dry during the rain. Figure 2 shows a photograph of the radome used in the measurements [1]. The site for these measurements was located approximately 8 km west of Billings Logan International Airport, Billings, MT, USA. The antenna was magnetically attached to a 10 cm × 10 cm × 1.6 mm metal plate which was taped to a 20 cm × 10 cm × 5 cm horizontally flat cement brick.

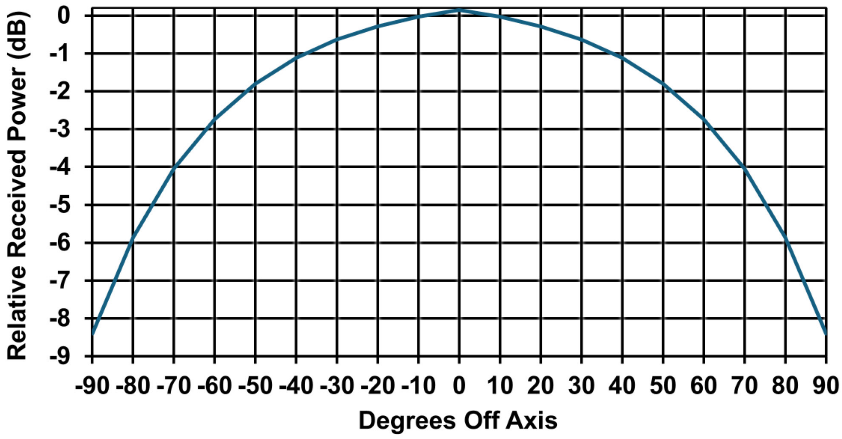

Figure 1. Relative received elevation power pattern for the GPS antenna.

Figure 2. The fiberglass hemispherical radome is leveled and centered over the GPS antenna [1].

Unlike the azimuth and elevation angle restrictions for GPS satellite SV 29 in [1], the received GPS azimuth and elevation angles in these measurements are not restricted. These restrictions have been relaxed because the normalized antenna elevation gain pattern from (1) is included, and the blockage angles are specified more accurately. Specifically, a vehicle created blockage at elevation angles of approximately $0^{\circ} \leq EL \leq 25^{\circ}$ and azimuth angles of approximately $70^{\circ} \leq AZ \leq 150^{\circ}$. Furthermore, low-elevation contamination at elevation angles of approximately $0^{\circ} \leq EL \leq 15^{\circ}$ can produce large, transmitted signal strength losses greater than 3 dB.

This technique assumes that the transmitted satellite signal strength from each GPS satellite is constant during measurements. This is a valid assumption since the measured GPS received power has been found to be highly repeatable, as tested for different satellites of three different block types [10] [11]. Therefore, the GPS transmit power (L1 C/A) of the full constellation was successfully estimated. However, there is still a minor potential limitation since variations in the GPS satellite transmission power could influence the calculated power loss. Signal power levels in the present measurements were collected for approximately 27 minutes to characterize the power transmission properties through the light rain.

The rain rate at the site was measured by a tipping-bucket-type rain gauge as described in [1]. During the light rain event, the rain gauge produced 3 signals at 6:29 p.m., 6:34 p.m., and 6:42 p.m. GMT. Visually, the rain rate was less from 6:21 p.m. - 6:25 p.m. GMT. Then the rain rate increased from 6:25 p.m. - 6:45 p.m. GMT. The rain stopped at 6:45 p.m. GMT. The skies became mostly clear overhead (zenith) from 6:45 p.m. - 6:48 p.m. GMT. During this time, the radome surface was dry, and the rain clouds moved from overhead to the east and south of the site. From 6:21 p.m. - 6:45 p.m. GMT, the average rain rate was calculated to be $0.75\ \text{mm}\cdot\text{h}^{-1}$. This is considered light rain since this rain rate result is less than $2.5\ \text{mm}\cdot\text{h}^{-1}$ [8].

A rain rate of $0.75\ \text{mm}\cdot\text{h}^{-1}$ produces an approximate water-layer thickness of 0.021 mm on the radome, see [1]. Therefore, the calculated power transmission losses through the radome and water-layer thickness combination, the radome thickness alone, and the water-layer thickness alone are 0.26, 0.17, and 0.05 dB, respectively from [1]. The water-layer's power transmission loss on the radome (0.05 dB) is neglected because it is much less than the minimum measured power transmission losses during the light rain (~0.5 dB). The radome's power transmission loss is eliminated by subtracting the received power during the light rain from the received power when the radome surface is dry during the mostly clear skies overhead from 6:45 p.m. - 6:48 p.m. GMT.

The measured power transmission loss (TL) in dB through the light rain event is estimated as [1]

$$TL = P_{maxdB} - P_{dB} \tag{2}$$

where

TL: power transmission loss in dB,

P_{dB}: received power in dB,

P_{maxdB}: received maximum power in dB during the mostly clear skies.

The transmittivity (T) in percent is [1]

$$T = \frac{P}{P_{max}} \times 100 \quad (3)$$

where

$P = 10^{\frac{P_{dB}}{10}}$ and $P_{max} = 10^{\frac{P_{maxdB}}{10}}$.

A maximum uncertainty of 1 dB is estimated for the losses that include receiver variability, rain-gauge resolution, antenna-gain correction, and baseline subtraction.

3.2. Plots of Measurements for 8 GPS Satellites

Plots of power transmission loss and transmissivity (power transmission) for 8 GPS satellite signals are shown in **Figures 3-18** from the largest elevation angles to the smallest elevation angles. The strong temporal and spatial variability of these measurements are evident in these plots. Specifically, notice the different power transmission loss values for **Figure 3**, **Figure 5**, **Figure 7**, **Figure 9**, **Figure 11**, **Figure 13**, **Figure 15**, and **Figure 17**. Furthermore, notice the different transmissivity values for **Figure 4**, **Figure 6**, **Figure 8**, **Figure 10**, **Figure 12**, **Figure 14**, **Figure 16**, and **Figure 18**. The measured power transmission loss and transmissivity equations are given in [1]. The normalized antenna elevation gain pattern from (1) is included in these measurements. Blockage at the site is minimized with elevation angles closest to zenith (EL = 90˚). The measured values are shown in blue, and the exponential smoothed values [1] are shown in orange. The smoothing process filters out the high-frequency signals to highlight the macroscopic signal degradation by the atmosphere.

The exponential smoothed curve is calculated by Microsoft's Excel Data Analysis Toolpak with a smoothing constant (α) of 0.8. The smoothing formula is [1]

$$P_{t+1} = \alpha P_t + (1-\alpha) P_{t-1} \quad (4)$$

where

P_{t+1}: next power value in dB,

P_{t-1}: previous power value in dB,

P_t: current power value in dB,

α: smoothing constant,

t: discrete time in s.

Figure 3 shows the measured power transmission loss in dB for GPS satellite SV 29. As shown in **Figure 3**, the smoothed maximum power transmission loss caused by the light rain is approximately 2.2 dB. **Figure 4** shows the measured transmissivity in percent for the light rain event for GPS satellite SV 29. Measurements in **Figure 4** show that the smoothed minimum transmissivity caused by the light rain is approximately 62%.

Figure 5 shows the measured power transmission loss in dB for GPS satellite SV 5. As shown in **Figure 5**, the smoothed maximum power transmission loss caused by the light rain is approximately 1.4 dB. **Figure 6** shows the measured transmissivity in percent for the light rain event for GPS satellite SV 5. Measurements in **Figure 6** show that the smoothed minimum transmissivity caused by the light rain is approximately 74%.

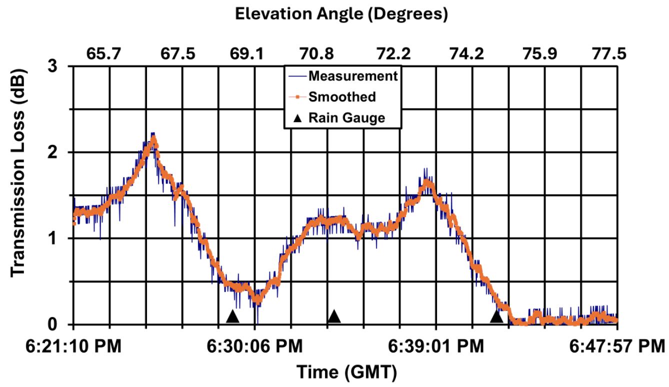

Figure 3. Measured (blue) and smoothed (orange) time plots of power transmission loss for the radome-covered GPS antenna during the light rain (0.75 mm·h^{-1}) for GPS satellite SV 29. The azimuth angles decreased from 307.7˚ to 304.3˚. The skies were mostly clear overhead from 6:45 p.m. - 6:48 p.m. GMT with a dry radome surface.

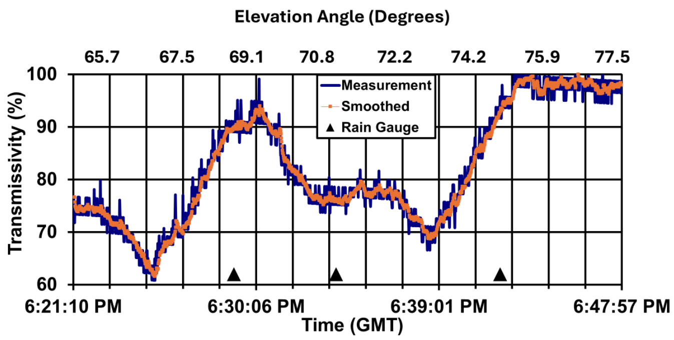

Figure 4. Measured (blue) and smoothed (orange) time plots of transmissivity for the radome-covered GPS antenna during the light rain (0.75 mm·h^{-1}) for GPS satellite SV 29. The azimuth angles decreased from 307.7˚ to 304.3˚. The skies were mostly clear overhead from 6:45 p.m. - 6:48 p.m. GMT with a dry radome surface.

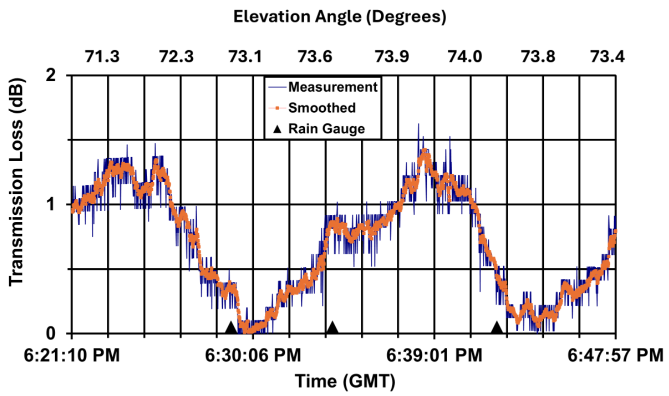

Figure 5. Measured (blue) and smoothed (orange) time plots of power transmission loss for the radome-covered GPS antenna during the light rain (0.75 mm·h^{-1}) for GPS satellite SV 5. The azimuth angles decreased from 138.6˚ to 93.9˚. The skies were mostly clear overhead from 6:45 p.m. - 6:48 p.m. GMT with a dry radome surface.

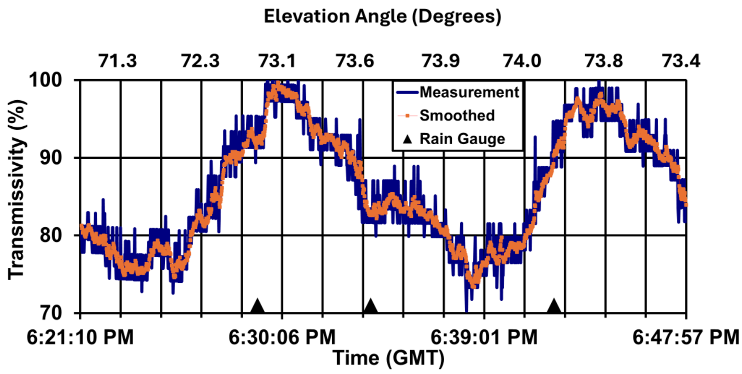

Figure 6. Measured (blue) and smoothed (orange) time plots of transmissivity for the radome-covered GPS antenna during the light rain (0.75 mm·h^{-1}) for GPS satellite SV 5. The azimuth angles decreased from 138.6˚ to 93.9˚. The skies were mostly clear overhead from 6:45 p.m. - 6:48 p.m. GMT with a dry radome surface.

Figure 7 shows the measured power transmission loss in for GPS satellite SV 20. As shown in Figure 7, the smoothed maximum power transmission loss caused by the light rain is approximately 1.7 dB. Figure 8 shows the measured transmissivity in percent for the light rain event for GPS satellite SV 20. Measurements in Figure 8 show that the smoothed minimum transmissivity caused by the light rain is approximately 68%.

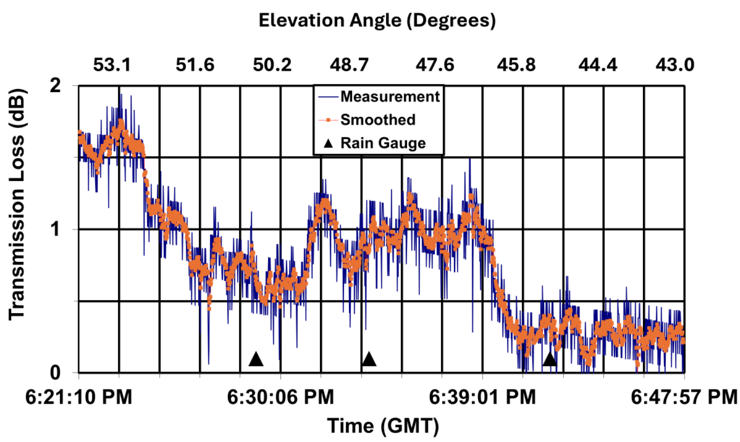

Figure 7. Measured (blue) and smoothed (orange) time plots of power transmission loss for the radome-covered GPS antenna during the light rain (0.75 mm·h^{-1}) for GPS satellite SV 20. The azimuth angles decreased from 60.7˚ to 54.1˚. The skies were mostly clear overhead from 6:45 p.m. - 6:48 p.m. GMT with a dry radome surface.

Figure 9 shows the measured power transmission loss in dB for GPS satellite SV 25. As shown in Figure 9, the smoothed maximum power transmission loss caused by the light rain is approximately 2.4 dB. Figure 10 shows the measured transmissivity in percent for the light rain event for GPS satellite SV 25. Measurements in Figure 10 show that the smoothed minimum transmissivity caused by the light rain is approximately 61%.

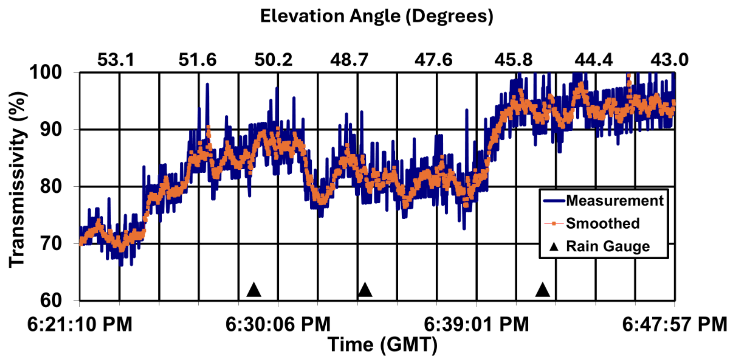

Figure 8. Measured (blue) and smoothed (orange) time plots of transmissivity for the radome-covered GPS antenna during the light rain (0.75 mm·h^{-1}) for GPS satellite SV 20. The azimuth angles decreased from 60.7˚ to 54.1˚. The skies were mostly clear overhead from 6:45 p.m. - 6:48 p.m. GMT with a dry radome surface.

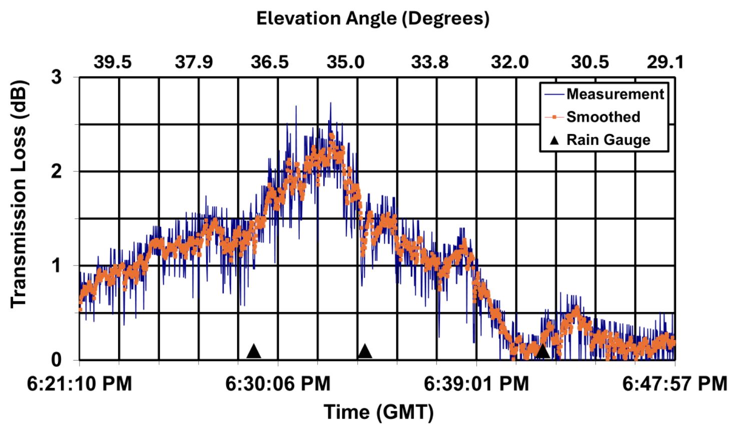

Figure 9. Measured (blue) and smoothed (orange) time plots of power transmission loss for the radome-covered GPS antenna during the light rain (0.75 mm·h^{-1}) for GPS satellite SV 25. The azimuth angles increased from 209.1˚ to 216.5˚. The skies were mostly clear overhead from 6:45 p.m. - 6:48 p.m. GMT with a dry radome surface.

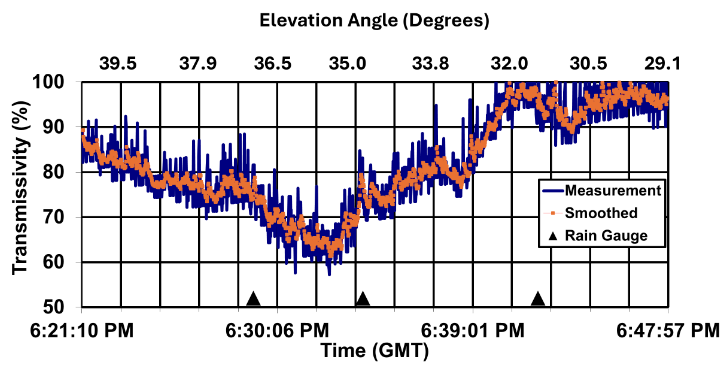

Figure 10. Measured (blue) and smoothed (orange) time plots of transmissivity for the radome-covered GPS antenna during the light rain (0.75 mm·h^{-1}) for GPS satellite SV 25. The azimuth angles increased from 209.1˚ to 216.5˚. The skies were mostly clear overhead from 6:45 p.m. - 6:48 p.m. GMT with a dry radome surface.

Figure 11 shows the measured power transmission loss in dB for GPS satellite SV 11. As shown in Figure 11, the smoothed maximum power transmission loss caused by the light rain is approximately 7 dB. Figure 12 shows the measured transmissivity in percent for the light rain event for GPS satellite SV 11. Measurements in Figure 12 show that the smoothed minimum transmissivity caused by the light rain is approximately 25%. The large power transmission loss values (>3 dB) and the small transmissivity values (<50%) show that these measurements are impacted by the blockage from the vehicle at elevation angles of approximately $0^\circ \le EL \le 25^\circ$ and azimuth angles of approximately $70^\circ \le AZ \le 150^\circ$ (see Section 3.1).

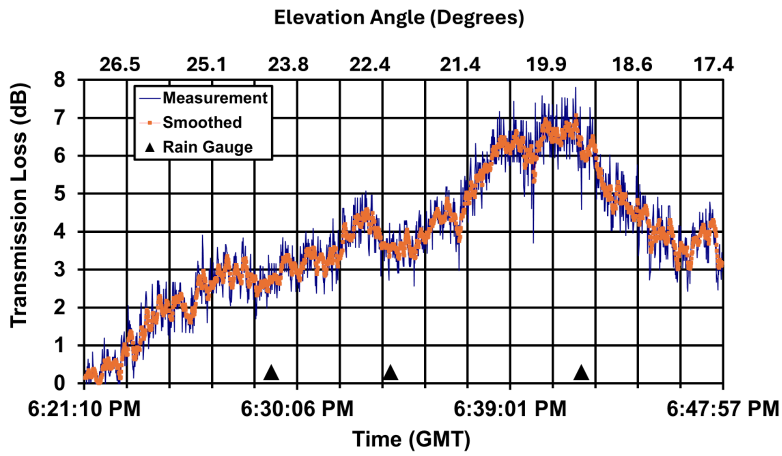

Figure 11. Measured (blue) and smoothed (orange) time plots of power transmission loss for the radome-covered GPS antenna during the light rain (0.75 mm·h^{-1}) for GPS satellite SV 11. The azimuth angles increased from 67.5˚ to 74.1˚. The skies were mostly clear overhead from 6:45 p.m. - 6:48 p.m. GMT with a dry radome surface.

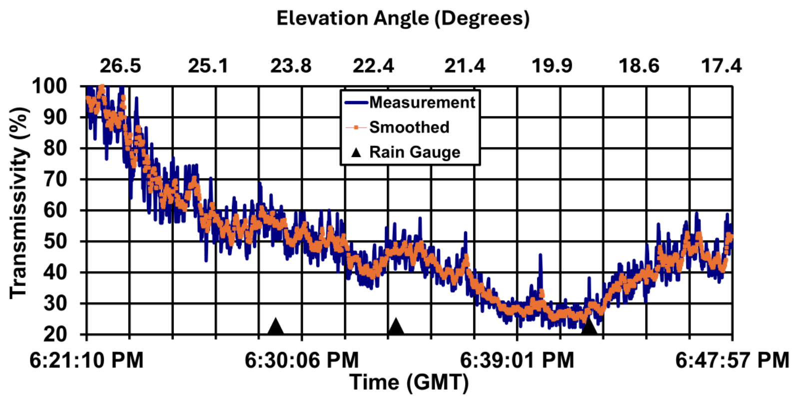

Figure 12. Measured (blue) and smoothed (orange) time plots of transmissivity for the radome-covered GPS antenna during the light rain (0.75 mm·h^{-1}) for GPS satellite SV 11. The azimuth angles increased from 67.5˚ to 74.1˚. The skies were mostly clear overhead from 6:45 p.m. - 6:48 p.m. GMT with a dry radome surface.

Figure 13 shows the measured power transmission loss in dB for GPS satellite SV 18. As shown in Figure 13, the smoothed maximum power transmission loss caused by the light rain is approximately 4.6 dB. Figure 14 shows the measured transmissivity in percent for the light rain event for GPS satellite SV 18. Measurements in Figure 14 show that the smoothed minimum transmissivity caused by the light rain is approximately 40%. The large power transmission loss values (>3 dB) and the small transmissivity values (<50%) show that these measurements are impacted by low-elevation contamination.

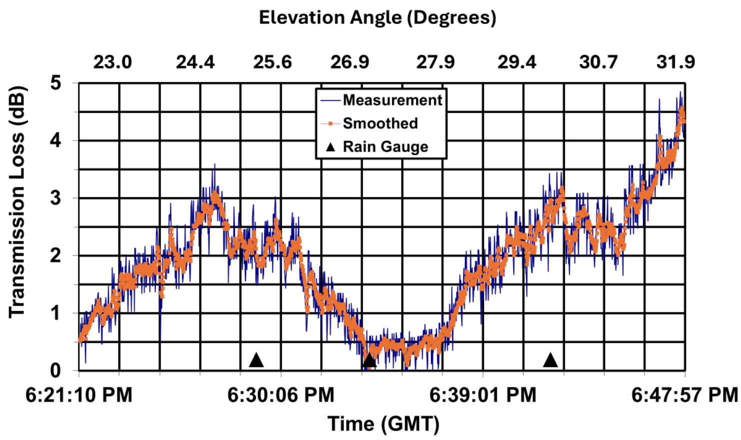

Figure 13. Measured (blue) and smoothed (orange) time plots of power transmission loss for the radome-covered GPS antenna during the light rain (0.75 mm·h^{-1}) for GPS satellite SV 18. The azimuth angles increased from 260.9˚ to 269.4˚. The skies were mostly clear overhead from 6:45 p.m.- 6:48 p.m. GMT with a dry radome surface.

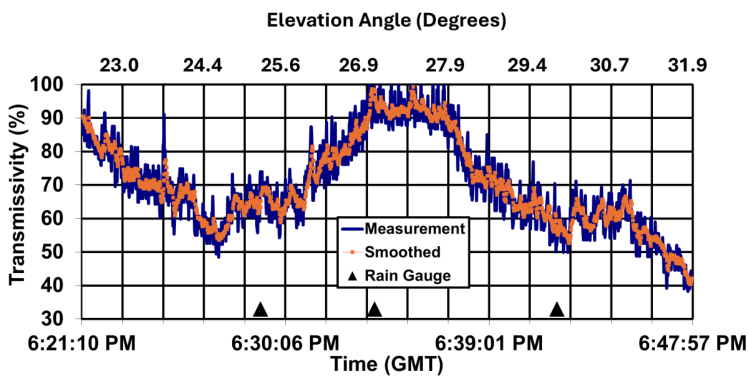

Figure 14. Measured (blue) and smoothed (orange) time plots of transmissivity for the radome-covered GPS antenna during the light rain (0.75 mm·h^{-1}) for GPS satellite SV 18. The azimuth angles increased from 260.9˚ to 269.4˚. The skies were mostly clear overhead from 6:45 p.m. - 6:48 p.m. GMT with a dry radome surface.

Figure 15 shows the measured power transmission loss in dB for GPS satellite SV 12. As shown in Figure 15, the smoothed maximum power transmission loss caused by the light rain is approximately 4.9 dB. Figure 16 shows the measured transmissivity in percent for the light rain event for GPS satellite SV 12. Measurements in Figure 16 show that the smoothed minimum transmissivity caused by the light rain is approximately 39%. The large power transmission loss values (>3 dB) and the small transmissivity values (<50%) show that these measurements are impacted by low-elevation contamination at elevation angles of approximately 0˚ ≤ *EL* ≤ 15˚ (see Section 3.1).

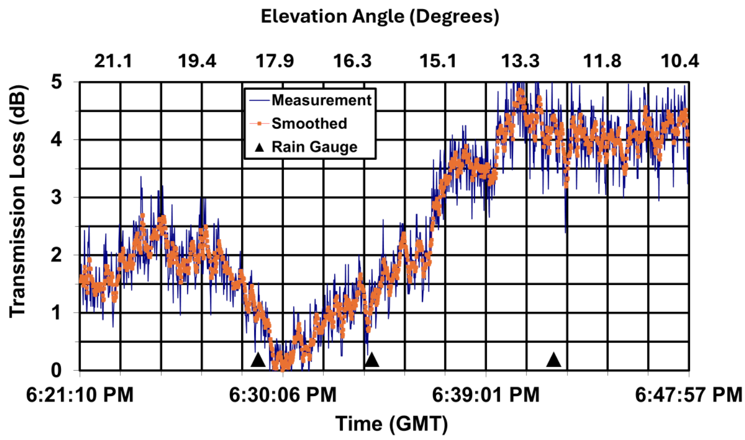

Figure 15. Measured (blue) and smoothed (orange) time plots of power transmission loss for the radome-covered GPS antenna during the light rain (0.75 mm·h^{-1}) for GPS satellite SV 12. The azimuth angles decreased from 182.7˚ to 180.8˚. The skies were mostly clear overhead from 6:45 p.m. - 6:48 p.m. GMT with a dry radome surface.

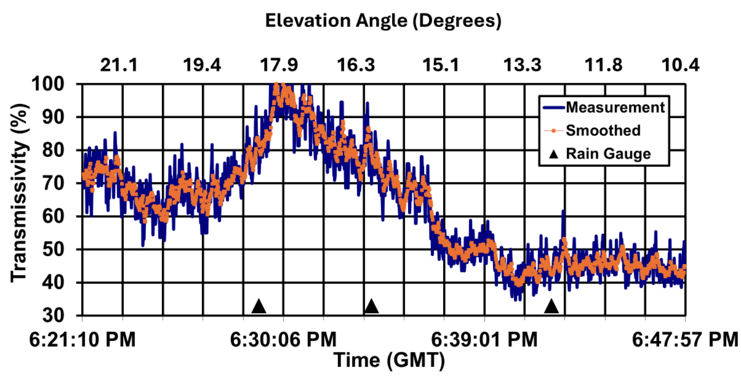

Figure 16. Measured (blue) and smoothed (orange) time plots of transmissivity for the radome-covered GPS antenna during the light rain (0.75 mm·h^{-1}) for GPS satellite SV 12. The azimuth angles decreased from 182.7˚ to 180.8˚. The skies were mostly clear overhead from 6:45 p.m. - 6:48 p.m. GMT with a dry radome surface.

Figure 17 shows the measured power transmission loss in dB for GPS satellite SV 26. As shown in Figure 17, the smoothed maximum power transmission loss caused by the light rain is approximately 5.7 dB. Figure 18 shows the measured transmissivity in percent for the light rain event for GPS satellite SV 26. Measurements in Figure 18 show that the smoothed minimum transmissivity caused by the light rain is approximately 35%. The large power transmission loss values (>3 dB) and the small transmissivity values (<50%) show that these measurements are impacted by low-elevation contamination at elevation angles of approximately 0˚ ≤ *EL* ≤ 15˚ (see Section 3.1).

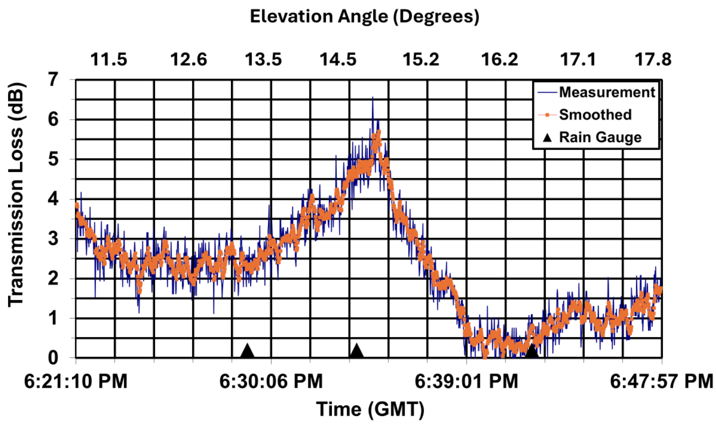

Figure 17. Measured (blue) and smoothed (orange) time plots of power transmission loss for the radome-covered GPS antenna during the light rain (0.75 mm·h^{-1}) for GPS satellite SV 26. The azimuth angles decreased from 322.3˚ to 314.2˚. The skies were mostly clear overhead from 6:45 p.m. - 6:48 p.m. GMT with a dry radome surface.

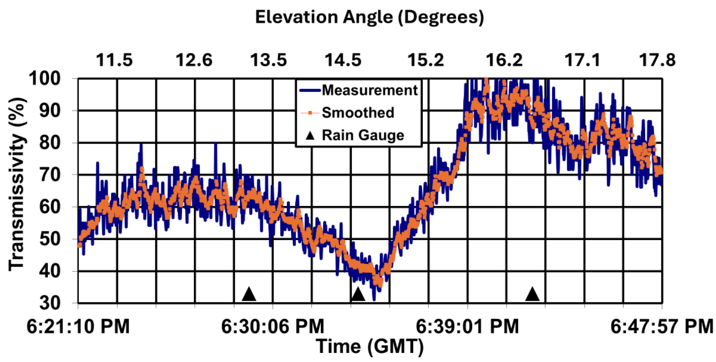

Figure 18. Measured (blue) and smoothed (orange) time plots of transmissivity for the radome-covered GPS antenna during the light rain (0.75 mm·h^{-1}) for GPS satellite SV 26. The azimuth angles decreased from 322.3˚ to 314.2˚. The skies were mostly clear overhead from 6:45 p.m. - 6:48 p.m. GMT with a dry radome surface.

3.3. Animations of Measurements for 8 GPS Satellites

As stated in Section 3.1, signal power levels from 8 GPS satellites were collected for approximately 27 minutes to characterize the power transmission properties through the light rain event. These 27 minutes of signal power levels are condensed to two 40 s animations in the two hyperlinks given below. Each animation shows the signal power levels as a function of elevation angle and azimuth angle (compass direction). The GPS signal strengths are represented by the size and colors (bar on right vertical axis) of the circles. Each GPS satellite (SV) is shown next to its respective circle. A progress bar at the bottom tracks the rainstorm progression in percent. The elapsed time of the rainstorm is given at the top. The 8 GPS satellite signal strengths are shown in the upper left corner.

The temporal and spatial variability of these measurements are evident in these animations. The measured power transmission loss and transmissivity (power transmission) equations are given in [1]. The normalized antenna elevation gain pattern given by (1) is included in these animations. Vehicle blockage and low-elevation contamination at the site is minimized with elevation angles closest to zenith (EL = 90˚). To filter out the high-frequency signals and to highlight the macroscopic signal degradation by the atmosphere, only the exponentially smoothed measurement values are visualized. The equation used for calculating the exponential smoothed values is given in [1].

The following hyperlink shows a 40 s animation of the measured power transmission loss in dB through the light rain event for 8 GPS satellite signals with an elapsed time of 27 minutes:

Transmission Loss (dB) Animation[1].

The following hyperlink shows a 40 s animation of the measured transmissivity (power transmission) in percent through the light rain event for 8 GPS satellite signals with an elapsed time of 27 minutes:

Transmissivity (%) Animation[2].

The two animations are generated using a custom Python script utilizing the Matplotlib and NumPy libraries. The script programmatically ingests the raw GPS dataset containing 1,600 temporal records of 1 s resolution for 8 concurrent GPS satellites (SVs 5, 11, 12, 18, 20, 25, 26, and 29). It maps the coordinate pairs of Azimuth Angle (0˚ to 360˚) and Elevation Angle (0˚ to 90˚) for all GPS satellites simultaneously onto a Cartesian coordinate system. To represent signal variability in real-time, the size and color of each GPS satellite marker are dynamically updated. To filter out the high-frequency signals and to highlight the macroscopic signal degradation by the atmosphere, only the exponentially smoothed measurement values are visualized. For the Transmission Loss animation, a sequential Yellow-Orange-Red (YlOrRd) colormap is used to represent signal transmission loss in decibels (dB). For the Transmissivity animation, a Yellow-Green-Blue (YlGnBu) colormap is used to show the percentage of signal transmission. Marker areas are normalized and scaled globally using a linear transformation mapping the dataset's absolute minimum and maximum values to bubble sizes between 120 and 900 square points. The script utilizes Matplotlib's FuncAnimation class to render 400 temporal frames sampled at 4 s intervals from the dataset, compiling them at a rate of 10 frames per second into a final 40 s publication-quality animation. A dynamic legend tracking current values for all GPS satellites, high-contrast text labels, and a bottom-aligned progress bar indicating GMT timestamps and percentage completion are integrated into the multi-panel layout using GridSpec.

4. Impact of GPS Signal Degradation by Rain

Tropospheric particles degrade GPS signals by depolarization and attenuation [6], [12]-[14]. Understanding and quantifying these depolarization and attenuation effects are necessary for optimal GPS use and accuracy. As shown in Section 3, precipitation in the form of light rain causes GPS signal degradation. The results

[1]https://youtu.be/FqIQtUu4WA8.

[2]https://www.youtube.com/watch?v=5HvX5tV4g90.

show that the GPS power transmission loss and transmissivity (power transmission) through the light rain are very spatially and temporally variable. This confirms that light rain is difficult to model because it is rarely uniform in time and space. Therefore, further real-time GPS-T measurements during light rain would help to quantify these effects. Furthermore, continued research involving more GPS and GNSS satellites and higher rain rates is needed to determine the usefulness of this technique.

This GPS-T technique could potentially improve GNSS-derived perceptible water vapor (PWV) measurements during rainfall events [15]-[20] by including the power transmission loss by raindrops. Although this idea is speculative, it may be worthwhile pursuing its usefulness with future research.

In addition, the GPS-T technique could potentially be used to detect ice crystals in clouds or clear air by measuring the depolarization of GPS signals. Attenuation by ice at L-band is minimal [8] [21] [22] and is therefore not relevant for ice crystal detection. Detecting ice crystals in clouds is important as Meng and Bi state [23], "Ice clouds are an essential component of the Earth's atmosphere" and "These results highlight the applicability for ice cloud remote sensing and its potential value for improving climate-related applications." Detecting ice crystals in clear air is also relevant as Gossard and Strauch state [24], "The depolarization of satellite signals under conditions that occasionally are visually 'clear' suggests that such events may be associated with ice crystals." Furthermore, depolarization measurements can reveal much about the freezing level by exploiting the bright-band phenomenon, where high reflectivity occurs just below the zero-degree isotherm. This occurs because of the transition of ice to water [25] and the change in shape as particles melt [26]. Based on depolarization measurements, Wexler concluded that shape changes for about 1.5 dB of enhancement. Kerker, Langleben and Gunn [27] and Warner [28] found that even a very thin water coating is sufficient to make the scatterer behave like a water droplet of the same mass. By monitoring the height region containing the freezing level, Lhermitte and Atlas [29] found that ice cloud begins to precipitate because the bright-band phenomenon depends on particles falling through the freezing level. Their measurements occurred during a light rain (1 $mm \cdot h^{-1}$) using a vertically pointing radar with a wavelength of $\lambda = 3.2$ cm, which corresponds to a frequency of approximately 9.4 GHz. Perhaps, using GPS-T with integrated GNSS tomography [30] could enhance detecting ice crystals.

5. Conclusions

Using 8 GPS orbital tracks improves the spatial and temporal resolution of the GPS-T measurements through the light rain event compared to using only 1 GPS orbital track in [1]. This is important since GPS is designed to provide continuous positioning and timing information anywhere in the world under all weather conditions [31] [32]. Quantifying power transmission losses through rain is necessary for optimal GPS use and accuracy. The results presented here provide received power variations of GPS L1 signals caused by light rain from 8 GPS satellites. These measurements show further potential for estimating power transmission loss and transmissivity (power transmission) of GPS signals through rain. Future studies would include more theoretical modeling of GPS-T.

To account for the antenna elevation gain pattern, the received GPS signals are added to the absolute value of the normalized antenna elevation gain pattern as given by (1). In contrast, the normalized antenna azimuth gain pattern is not included in this study because it is assumed to be approximately constant. Future studies would include the normalized antenna azimuth gain pattern. Incorporating both elevation and azimuth gain patterns would produce a 3-dimensional antenna gain pattern. Consequently, a 3-dimensional antenna gain pattern would improve the accuracy of the GPS-T measurements.

During the measurements, it was assumed that transmitted GPS signal strengths were constant, see Section 3. Further measurements of transmitted GPS satellite signal strengths during clear sky conditions are needed to quantify the stability of transmitted GPS signal strengths. Additional GPS-T measurements for different rain rates and more GPS and GNSS signals are needed to determine the validity and usefulness of this technique. This GPS-T technique could potentially improve GNSS-derived PWV measurements during rainfall events by including the power transmission loss by raindrops. Future research will determine if this idea is feasible. Another possible use of this technique is to potentially detect ice crystals by measuring the depolarization of GPS signals. Lastly, this GPS-T technique could be expanded for GNSS signals. The key benefit of such an expansion, by leveraging signals from multiple constellations, is to improve spatial and temporal resolution.

Acknowledgements

The authors would like to thank J. Plance, M. Barnhart, D. Carter, S. Miller, and A. Barber of Montana State University Billings for their critical involvement in this research. This work was supported by the Montana State University Billings Mathematics Department. The authors would also like to thank the anonymous reviewers for their very valuable comments and suggestions.

Conflicts of Interest

The authors declare no conflicts of interest regarding the publication of this paper.

References

[1] Jacobson, M.D. (2026) GPS Transmissivity through Light Rain. *Positioning*, **17**, 1-11. https://doi.org/10.4236/pos.2026.171001

[2] Balasubramaniam, R. and Ruf, C. (2020) Characterization of Rain Impact on L-Band GNSS-R Ocean Surface Measurements. *Remote Sensing of Environment*, **239**, Article ID: 111607. https://doi.org/10.1016/j.rse.2019.111607

[3] Taur, R.R. (1975) Rain Depolarization Measurements on a Satellite-Earth Propagation Path at 4 GHz. *IEEE Transactions on Antennas and Propagation*, **23**, 854-858.

https://doi.org/10.1109/tap.1975.1141200

[4] Hao, A., Wei, Y., Heng, B., Wenjun, L., Yang, F. and Ying, H. (2013) Research on Retrieval of Rain Rate Using Polarimetric GNSS Signals. *Proceedings of the* 2013 *the International Conference on Remote Sensing*, *Environment and Transportation Engineering* (*RSETE* 2013), Nanjing, 26-28 July 2013, 440-443.

[5] Kobayashi, T. (1976) Pre-Estimation of Cross-Polarization Discrimination Due to Rain. *Journal of the Radio Research Laboratories* (*Japan*), **23**, 47-64. https://ui.adsabs.harvard.edu/abs/1976RaRLJ..23...47K/abstract

[6] Flock, W.L. (1983) Propagation Effects on Satellite Systems at Frequencies below 10 GHz. A Handbook for Satellite Systems Design. NASA, 1108.

[7] Stutzman, W.L. (1993) Polarization in Electromagnetic Systems. Artech House, Inc.

[8] Ulaby, F.T., Moore, R.K. and Fung, A.K. (1981) Microwave Remote Sensing, Active and Passive. Vol. 1, Addison-Wesley Publishing Company, Inc.

[9] Jacobson, M.D. (2014) Estimating Snow Water Equivalent for a Slightly Tilted Snow-Covered Prairie Grass Field by GPS Interferometric Reflectometry. *EURASIP Journal on Advances in Signal Processing*, **2014**, Article No. 61. https://doi.org/10.1186/1687-6180-2014-61

[10] Wang, T., Ruf, C.S., Block, B., McKague, D.S. and Gleason, S. (2019) Design and Performance of a GPS Constellation Power Monitor System for Improved CYGNSS L1B Calibration. *IEEE Journal of Selected Topics in Applied Earth Observations and Remote Sensing*, **12**, 26-36. https://doi.org/10.1109/jstars.2018.2867773

[11] Wang, T., Ruf, C., Block, B., McKague, D. and Gleason, S. (2018) Characterization of GPS L1 EIRP: Transmit Power and Antenna Gain Pattern. *ION GNSS*+, *The International Technical Meeting of the Satellite Division of the Institute of Navigation*, Miami, September 2018, 2879-2890. https://doi.org/10.33012/2018.16101

[12] Solheim, F.S., Vivekanandan, J., Ware, R.H. and Rocken, C. (1999) Propagation Delays Induced in GPS Signals by Dry Air, Water Vapor, Hydrometeors, and Other Particulates. *Journal of Geophysical Research*: *Atmospheres*, **104**, 9663-9670. https://doi.org/10.1029/1999jd900095

[13] MacGouran, G., Lachapelle, G. and Nayak, R. (2001) Overview of GNSS Signal Degradation Phenomena. *International Symposium on Kinematic Systems in Geodesy*, *Geomatics and Navigation*, Banff, 5-8 June 2001, 87-100. https://www.researchgate.net/publication/242078138_OVERVIEW_OF_GNSS_SIGNAL_DEGRADATION_PHENOMENA

[14] Levis, C.A., Johnson, J.T. and Teixeira, F.L. (2010) Radiowave Propagation: Physics and Applications. John Wiley & Sons, Inc.

[15] Barindelli, S., Realini, E., Venuti, G., Fermi, A. and Gatti, A. (2018) Detection of Water Vapor Time Variations Associated with Heavy Rain in Northern Italy by Geodetic and Low-Cost GNSS Receivers. *Earth*, *Planets and Space*, **70**, Article No. 28. https://doi.org/10.1186/s40623-018-0795-7

[16] Li, J., Li, F., Zhang, B., Yao, Y., Liu, L., Huang, L., *et al.* (2026) Case Study on Zenith Hydrostatic Delay Calibration Models for Forecast Vienna Mapping Function 3 and Their Impact on GNSS Precipitable Water Vapor Retrieval. *IEEE Transactions on Geoscience and Remote Sensing*, **64**, 1-12. https://doi.org/10.1109/tgrs.2026.3655097

[17] Yao, C., Nie, Z., You, H., Shum, C.K., Wang, H., Xiong, S., *et al.* (2026) A Daily Drought Index Integrating GNSS Precipitable Water Vapor and Precipitation Observables. *IEEE Transactions on Geoscience and Remote Sensing*, **64**, 1-12. https://doi.org/10.1109/tgrs.2026.3678957

[18] Xu, J., Liu, Z., Wimmers, A. and Velden, C. (2026) Independent Validation of Total Precipitable Water from Morphed Integrated Microwave Imagery at CIMSS: A Global Study Using GNSS and Radiosonde Measurements. *IEEE Transactions on Geoscience and Remote Sensing*, **64**, 1-13. https://doi.org/10.1109/tgrs.2026.3656168

[19] Jin, Z., Yu, Z., Lu, Z., Chen, F., Hao, S., Xu, Y., *et al.* (2026) On the Potential of Using GNSS-Derived Precipitable Water Vapor from 5G Base Stations to Improve the Model for Typhoon Precipitation Forecasting. *IEEE Journal of Selected Topics in Applied Earth Observations and Remote Sensing*, **19**, 9739-9752. https://doi.org/10.1109/jstars.2026.3669007

[20] Zhu, D., Li, W., Zhang, K., Hu, Q., He, P., Zhang, L., *et al.* (2026) A Multichannel CNN-LSTM-Based Prediction Model for Precipitable Water Vapor in a Region with a Single GNSS Station. *IEEE Journal of Selected Topics in Applied Earth Observations and Remote Sensing*, **19**, 3502-3514. https://doi.org/10.1109/jstars.2025.3649502

[21] Ulaby, F.T., Moore, R.K. and Fung, A.K. (1986) Microwave Remote Sensing, Active and Passive. Vol. 3, Artech House.

[22] Jacobson, M.D. (2010) Snow-Covered Lake Ice in GPS Multipath Reception—Theory and Measurement. *Advances in Space Research*, **46**, 221-227. https://doi.org/10.1016/j.asr.2009.10.013

[23] Meng, Y. and Bi, L. (2026) Evaluation of Ice Crystal Scattering Models Using Polarimetric Observations. *IEEE Geoscience and Remote Sensing Letters*, **23**, Article ID: 1001205. https://doi.org/10.1109/lgrs.2026.3694098

[24] Gossard, E.E. and Strauch, R.G. (1983) Radar Observation of Clear Air and Clouds. Elsevier Science Ltd.

[25] Austin, P.M. and Bemis, A.C. (1950) A Quantitative Study of the “Bright Band” in Radar Precipitation Echoes. *Journal of Meteorology*, **7**, 145-151. https://doi.org/10.1175/1520-0469(1950)007<0145:aqsotb>2.0.co;2

[26] Wexler, R. (1955) An Evaluation of the Physical Effects in the Melting Layer. *Proceedings of Fifth Weather Radar Conference*, Fort Monmouth, 12-15 September 1955, 329-334.

[27] Kerker, M., Langleben, M.P. and Gunn, K.L.S. (1951) Scattering of Microwaves by a Melting, Spherical Ice Particle. *Journal of Meteorology*, **8**, Article No. 424. https://doi.org/10.1175/1520-0469(1951)008<0424:sombam>2.0.co;2

[28] Warner, C. (1977) Calculations of Backscattering and Depolarization by Wet Hailstones at 2.88 GHz. Scientific Report 17w-90, McGill University, 57 p.

[29] Lhermitte, R.M. and Atlas, D. (1963) Doppler Fall Speed and Particle Growth in Stratiform Precipitation. *Proceedings Tenth Weather Radar Conference*, Boston, 22-25 April 1963, 297-302.

[30] Cegla, A., Taszarek, M., Kryza, M., Rohm, W. and Moeller, G. (2026) Detecting Signatures of Giant Hail Events with Integrated GNSS Tomography: A Case Study over Southern Poland. *IEEE Transactions on Geoscience and Remote Sensing*, **64**, 1-5. https://doi.org/10.1109/tgrs.2026.3659018

[31] El-Rabbany, A. (2006) Introduction to GPS, the Global Positioning System. 2nd Edition, Artech House.

[32] Bonafoni, S. and Biondi, R. (2016) The Usefulness of the Global Navigation Satellite Systems (GNSS) in the Analysis of Precipitation Events. *Atmospheric Research*, **167**, 15-23. https://doi.org/10.1016/j.atmosres.2015.07.011